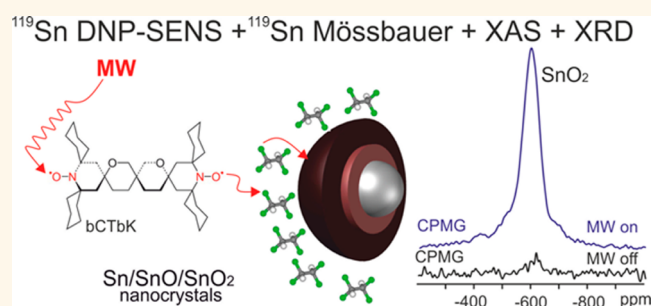


# Unraveling the Core–Shell Structure of Ligand-Capped Sn/SnO<sub>x</sub> Nanoparticles by Surface-Enhanced Nuclear Magnetic Resonance, Mössbauer, and X-ray Absorption Spectroscopies

Loredana Protesescu,<sup>†,‡,▲</sup> Aaron J. Rossini,<sup>§,▲</sup> Dominik Kriegner,<sup>#</sup> Maxence Valla,<sup>†</sup> Antoine de Kergommeaux,<sup>‡</sup> Marc Walter,<sup>†,‡</sup> Kostiantyn V. Kravchyk,<sup>†,‡</sup> Maarten Nachtegaal,<sup>¶</sup> Julian Stangl,<sup>#</sup> Bernard Malaman,<sup>||</sup> Peter Reiss,<sup>‡</sup> Anne Lesage,<sup>§</sup> Lyndon Emsley,<sup>§</sup> Christophe Copéret,<sup>†</sup> and Maksym V. Kovalenko<sup>†,‡,\*</sup>

<sup>†</sup>Institute of Inorganic Chemistry, Department of Chemistry and Applied Biosciences, ETH Zürich CH-8093, Switzerland, <sup>‡</sup>Empa-Swiss Federal Laboratories for Materials Science and Technology, Dübendorf CH-8600, Switzerland, <sup>§</sup>Centre de RMN à Très Hauts Champs, Institut de Sciences Analytiques (CNRS/ENS Lyon/UCB Lyon 1), Université de Lyon, 69100 Villeurbanne, France, <sup>‡</sup>Laboratoire d'Electronique Moléculaire, Organique et Hybride, CEA Grenoble, INAC, SPrAM UMR 5819 (CEA/CNRS/UJF-Grenoble 1), 38054 Grenoble cedex 9, France, <sup>||</sup>Institut Jean Lamour, Université de Lorraine, UMR 7198, 54506 Vandoeuvre-lès-Nancy Cedex, France, <sup>¶</sup>Paul Scherrer Institute, 5232 Villigen PSI, Switzerland, and <sup>#</sup>Institute of Semiconductor and Solid State Physics, Johannes Kepler University Linz, A-4040 Linz, Austria. <sup>▲</sup>These authors contributed equally to this work.

**ABSTRACT** A particularly difficult challenge in the chemistry of nanomaterials is the detailed structural and chemical analysis of multicomponent nano-objects. This is especially true for the determination of spatially resolved information. In this study, we demonstrate that dynamic nuclear polarization surface-enhanced solid-state NMR spectroscopy (DNP-SENS), which provides selective and enhanced NMR signal collection from the (near) surface regions of a sample, can be used to resolve the core–shell structure of a nanoparticle. Li-ion anode materials, monodisperse 10–20 nm large tin nanoparticles covered with a ~3 nm thick layer of native oxides, were used in this case study. DNP-SENS selectively enhanced the weak <sup>119</sup>Sn NMR signal of the amorphous surface SnO<sub>2</sub> layer. Mössbauer and X-ray absorption spectroscopies identified a subsurface SnO phase and quantified the atomic fractions of both oxides. Finally, temperature-dependent X-ray diffraction measurements were used to probe the metallic β-Sn core and indicated that even after 8 months of storage at 255 K there are no signs of conversion of the metallic β-Sn core into a brittle semiconducting α-phase, a phase transition which normally occurs in bulk tin at 286 K (13 °C). Taken together, these results indicate that Sn/SnO<sub>x</sub> nanoparticles have core/shell1/shell2 structure of Sn/SnO/SnO<sub>2</sub> phases. The study suggests that DNP-SENS experiments can be carried on many types of uniform colloidal nanomaterials containing NMR-active nuclei, in the presence of either hydrophilic (ion-capped surfaces) or hydrophobic (capping ligands with long hydrocarbon chains) surface functionalities.



**KEYWORDS:** dynamic nuclear polarization · solid-state NMR · XAS · tin · nanoparticles · colloidal · core/shell structure · Li-ion batteries

With the increasing maturity of synthetic methods, there is a constantly growing demand for the reliable and accurate structural and compositional analysis of nanoscale inorganic materials. The major difficulties in characterization arise from broadening of the peaks in X-ray diffraction (XRD) patterns by reduced particle sizes, structural disorder or

amorphization, stoichiometric variations, and large surface areas, to mention just a few. For instance, the seemingly simple objects of this study, partially oxidized Sn nanoparticles (Sn/SnO<sub>x</sub> NPs), are inherently complex entities containing a crystalline metallic core, covered with a native layer of amorphous oxide shell, which is subsequently capped with surface ligands. Our interest

\* Address correspondence to mvkovalenko@ethz.ch.

Received for review December 11, 2013 and accepted February 1, 2014.

Published online February 01, 2014  
10.1021/nn406344n

© 2014 American Chemical Society

in Sn-based nanomaterials arises from their use as high-energy density anode materials for rechargeable Li-ion batteries.<sup>1,2</sup> Monodisperse and size-tunable Sn/SnO<sub>x</sub> NPs, synthesized from Sn amide precursors, represent an ideal system for both *ex situ* and *in situ* studies of size-dependent electrochemical lithiation.<sup>1,2</sup> We recently showed that these NPs with diameters down to 10 nm exhibit near-theoretical charge storage capacities and improved cycling stability, especially if compared to the larger (50–150 nm) and polydisperse Sn and SnO<sub>2</sub> NPs. However, very little information could be obtained with regard to the chemical identity of the surface oxide shell using the standard toolbox for characterization of nanoparticles, such as transmission electron microscopy (TEM) and X-ray diffraction (XRD). Besides the impact that surface oxides have on the Li-ion storage properties of nanoscopic Sn electrodes, the problem of characterizing surface and/or outermost, often amorphous, layers of nanomaterials is of generally much broader importance and requires complementary methods. In this study, we show that the well-known and reliable X-ray absorption (XAS) and <sup>119</sup>Sn Mössbauer spectroscopies can identify and quantify amorphous SnO and SnO<sub>2</sub> but cannot provide insight into the arrangement of these phases within the surface oxide shell. We thus employ an additional, local and nondestructive method that is *a priori* designed to yield surface-specific chemical information: a recently developed solid-state NMR technique known as dynamic nuclear polarization surface-enhanced NMR spectroscopy (DNP-SENS).<sup>3–5</sup>

Solid-state magic-angle spinning nuclear magnetic resonance (MAS NMR) serves as a powerful tool for characterizing structure and dynamics in solids, ranging from conventional inorganic materials to proteins. Previous MAS NMR and solution NMR investigations of sub-10 nm colloidal NPs (primarily semiconductors such as CdSe, CdTe, PbSe, etc.) have provided information about the internal structure of the NP cores<sup>6–8</sup> and about the organic ligand capping, including the ligand–NP equilibria in the liquid state.<sup>9–12</sup> One-dimensional MAS NMR spectra of semiconductor NPs are usually acquired with direct polarization NMR experiments. Such spectra primarily provide information about the bulk structure of the NPs and are usually inhomogeneously broadened by the distribution of atomic environments within the NPs. Surface-selective cross-polarization (CP, *i.e.*, <sup>1</sup>H→X magnetization transfers, where X = <sup>77</sup>Se, <sup>113</sup>Cd, <sup>207</sup>Pb, etc.) experiments on NPs can provide additional insight into the structure of the surface and/or outer layers of NPs.<sup>13</sup> However, CP experiments are generally challenging due to the low concentrations of surface sites and/or low specific surface areas, residual ligand dynamics that reduces heteronuclear <sup>1</sup>H–X dipolar couplings,<sup>7</sup> and, most importantly, the generally poor sensitivity of NMR spectroscopy. Additionally, broad peaks are usually observed in surface-selective experiments

because of surface disorder. The study of NPs by solid-state NMR would greatly benefit from signal enhancement techniques.

*In situ* high-field DNP is emerging as an extremely powerful method to enhance NMR signals *via* microwave (MW)-induced polarization transfer from unpaired electrons to nuclear spins.<sup>14,15</sup> While high-field DNP was initially applied for the studies of biomolecules, it has recently been shown by some of us that DNP could be used to enhance the NMR signals of surface species.<sup>3–5</sup> Typically, porous and nonporous solid materials are impregnated with solutions containing stable organic biradical polarizing agents.<sup>16,17</sup> MW irradiation then transfers the high polarization of the electrons to the protons of the solvent and other molecular species residing at the surface of the material. The enhanced proton polarization is transferred through CP to the desired heteronuclei (*i.e.*, <sup>13</sup>C, <sup>15</sup>N, <sup>27</sup>Al, <sup>29</sup>Si, etc.) located at/on the surface of the material.<sup>5,18–21</sup> <sup>1</sup>H DNP signal enhancements ( $\epsilon_H$ ) of a factor of 658 are theoretically possible, and with the best biradical polarizing agents, signal enhancements above 100 are now routinely obtained on 9.3 T spectrometers.<sup>22–24</sup> These large enhancements translate into a tremendous reduction in experiment time since time savings are proportional to  $\epsilon$ .<sup>2</sup> It is well-known in solid-state NMR that CP transfers from protons to heteronuclei are generally effective over distances less than ~1 nm, and therefore, *the DNP-enhanced CPMAS solid-state NMR spectra would selectively provide information about chemical nature of the surface region of the NP.*

Here we demonstrate that DNP-SENS<sup>5</sup> enables the rapid acquisition of CPMAS NMR spectra of the natural oxide coating and capping ligands on colloidal Sn/SnO<sub>x</sub> NPs. In particular, we determine a Sn/SnO/SnO<sub>2</sub> core/shell1/shell2 structure of the NPs by combining DNP-SENS with Mössbauer and X-ray absorption spectroscopies. DNP-SENS demonstrates that the outer shell of the NPs is made up exclusively of amorphous SnO<sub>2</sub>; XRD and TEM show a crystalline  $\beta$ -Sn core, and XAS and Mössbauer spectroscopies detect an interlayer of amorphous SnO and the atomic fraction of each of three phases. Furthermore, we show how the DNP-SENS experiments can be carried out for hydrophilic (ion-capped surfaces) and hydrophobic (capping ligands with long hydrocarbon chains) surface functionalities in various solvents, thus opening the way for future studies on a broad range of uniform colloidal nanomaterials containing NMR-active nuclei.

## RESULTS AND DISCUSSION

Monodisperse 10 and 18 nm colloidal Sn NPs with a standard size deviation below 10% (Figure S1, see Supporting Information) were synthesized according to a recently published method based on chemical reduction of Sn(II)-oleylamide in oleylamine as a solvent.<sup>1</sup> Oleate capping is applied postsynthetically

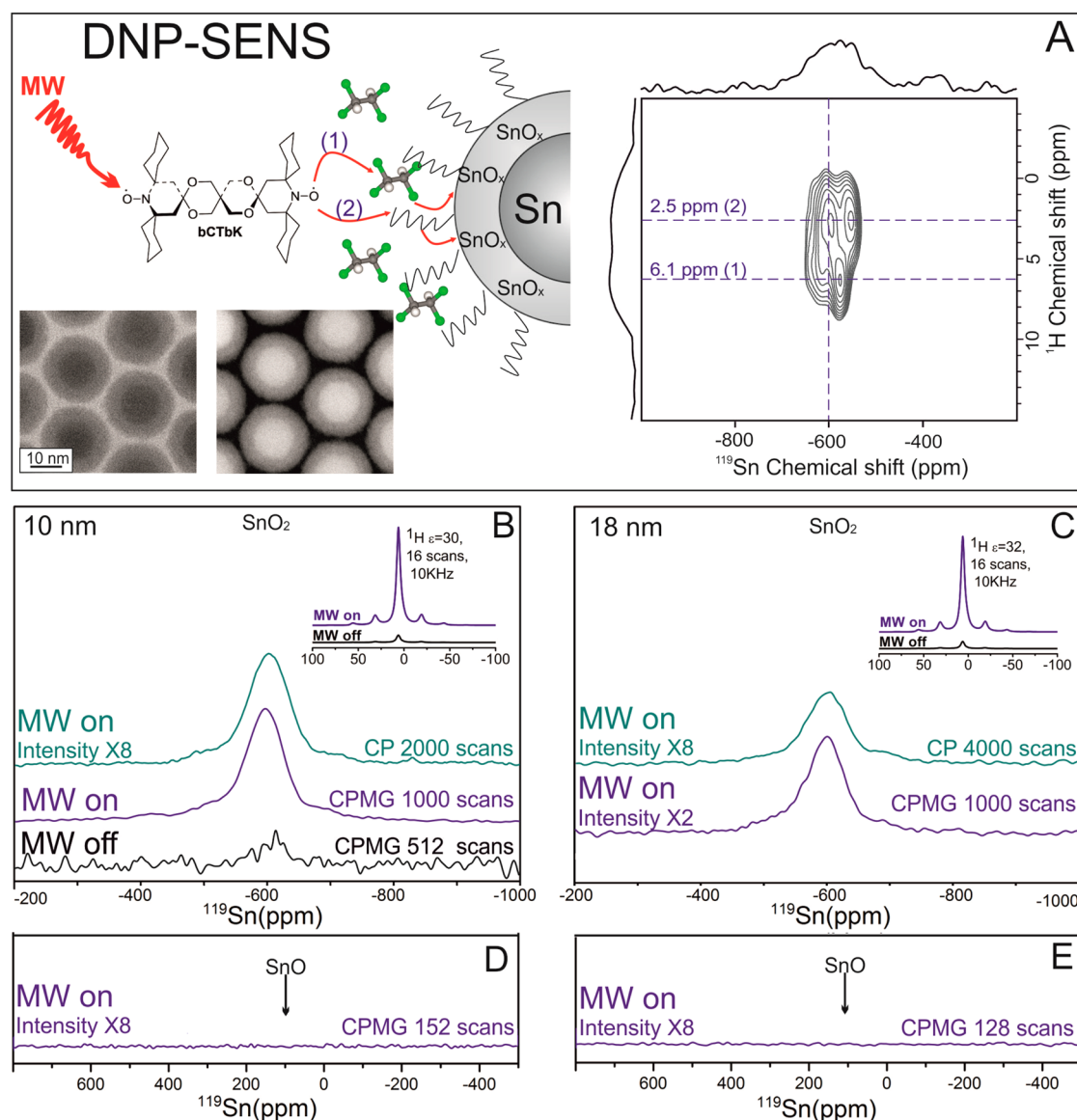
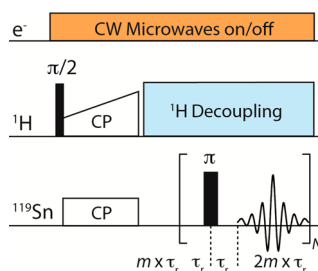


**Figure 1.** (A) Schematic representation of the DNP-SENS experiment used to enhance the signal of the Sn species on  $\text{Sn}/\text{SnO}_x$  NP surface via microwave (MW)-induced polarization transfer from electrons first to protons and then to Sn nuclei. Insets show a DNP-enhanced 2D  $^1\text{H}$ – $^{119}\text{Sn}$  HETCOR spectra and high-resolution bright-field STEM and high-angle annular dark-field STEM (HAADF-STEM) images of oleate-capped 10 nm  $\text{Sn}/\text{SnO}_x$  NPs. (B,C)  $^{119}\text{Sn}$  MAS DNP-SENS spectra for oleate-capped 10 and 18 nm  $\text{Sn}/\text{SnO}_x$  NPs suspended in TCE solutions of 12 mM bCTbK; MW off CP-CPMG (black line, 512 scans, 2 s recycle delay), MW on-CPMG (dark blue, 1000 scans, 3.5 s recycle delay), and MW on CP (green, 2000 scans, 3.5 s recycle delay). Inset show the MW off/MW on  $^1\text{H}$  echo solid-state NMR spectra. (D,E) Lack of detectable signal in the region relevant to  $\text{SnO}$ . CP-CPMG spectra are shown in their echo reconstructed form. They were obtained by summing the whole echoes of the FIDs in the time domain, followed by Fourier transform and application of a first-order phase correction.<sup>25,26</sup>

to ensure long-term chemical and colloidal stability. The completeness of the amine-to-carboxylate exchange is confirmed by FTIR spectroscopy (Figure S2). For the samples purified and handled in air, the presence of the surface oxide layers is apparent from high-resolution bright-field STEM and high-angle annular dark-field STEM (HAADF-STEM) images (insets in Figure 1A), while powder XRD detected only one crystalline phase, which is metallic  $\beta$ -Sn. This information raises several questions about the structure of the composite nanoparticle, the foremost concerning the composition of the native oxide capping.

**NMR Spectroscopy.** Prior to attempting DNP-enhanced experiments, we collected standard direct excitation  $^{119}\text{Sn}$  MAS NMR spectra recorded for 10 nm  $\text{SnO}_x$  NPs. A weak, broad peak was observed at  $\sim -600$  ppm, consistent with amorphous  $\text{SnO}_2$  (Figure S3, 38231 scans, 21 h). Note that no other signals were observed in the regions of 300 to  $-800$  ppm, where signals from  $\text{SnO}$  would be expected (see the NMR spectrum of bulk  $\text{SnO}$  in Figure S4). We also note that  $\beta$ -Sn cannot likely be observed due to a very large Knight shift anisotropy (KSA) with principal components of the shift tensor:<sup>27</sup>  $\delta_{11} = 46\,500$  ppm,  $\delta_{22} = -23\,250$  ppm,  $\delta_{33} = -23\,250$  ppm



**Scheme 1.** CP-CPMG pulse sequence utilized to acquire DNP-enhanced MAS  $^1\text{H}$ – $^{119}\text{Sn}$  CP-CPMG NMR spectra, where  $\tau_r$  is the rotor period and  $m$  and  $N$  are integers.<sup>32,33</sup>

(compare to  $\delta_{11} = -560$  ppm,  $\delta_{22} = -560$  ppm,  $\delta_{33} = -685$  ppm for  $\text{SnO}_2$ ). The low signal-to-noise ratios for NMR signals arising from the  $\text{SnO}_2$  components, obtained with long acquisition times (21 h, 38 231 scans!) indicate that these resonances are close to the detection limits and/or that the content of the  $\text{SnO}_2$  phase is very low. However, TEM images indicate that 10–60% of the NP volume consists of the amorphous oxide shell. Furthermore, Mössbauer spectra and XAS measurements below indicate that  $\sim 60$  atom % of the oxide overlayer is composed of  $\text{SnO}_2$ , suggesting that the main issue preventing the observation of the  $^{119}\text{Sn}$  NMR signals is the low sensitivity of NMR spectroscopy.

In contrast, with DNP-SENS, we were able to dramatically enhance the NMR signals of the outer  $\text{SnO}_2$  layer. In the case of oleate-capped  $\text{Sn}/\text{SnO}_x$  NPs, a highly concentrated solution of NPs ( $\sim 50\%$  NPs by volume) in 1,1,2,2-tetrachloroethane (TCE) is mixed with an equivalent volume of a 24 mM solution of the nitroxide-based organic biradical bCTbK (biscyclohexylpiperidinyloxybisketal)<sup>28,29</sup> in TCE. The mixing reduces the concentration of NPs within the sample by about a factor of 2. However, this dilution is more than offset by the large DNP sensitivity enhancements. The NPs were dispersed in the present case to prevent aggregation. Similarly, several studies have demonstrated that it is straightforward to apply DNP to silica and clay nanoparticles dispersed in or impregnated with aqueous biradical solutions.<sup>3,30,31</sup> bCTbK and TCE were chosen as the radical/solvent combination because of the hydrophobicity of oleate-capped  $\text{Sn}/\text{SnO}_x$  NPs and because this mixture routinely provides  $^1\text{H}$  DNP enhancement factors ( $\epsilon_{\text{H}}$ ) on the order of 100 at 9.4 T with sample temperatures of  $\sim 100$  K.<sup>28</sup> In order to transfer polarization from the electron spins to the proton spins of the solvent and oleate ligands, the sample is subjected to continuous-wave 263 GHz microwaves (gyrotron source,  $\sim 5$  W of MW power at the sample). The enhanced  $^1\text{H}$  polarization is then transferred through a CP step, to the X nuclei ( $^{119}\text{Sn}$  and  $^{13}\text{C}$  in this study). In order to maximize sensitivity of  $^{119}\text{Sn}$  MAS NMR signals, spectra were acquired with a Carr–Purcell–Meiboom–Gill (CPMG)<sup>32,33</sup> acquisition scheme after the CP transfer step (Scheme 1). In CPMG, a train of refocusing pulses is

applied to acquire a series of spin echoes. In the present case, the effective coherence lifetime ( $T_2'$ ) of the  $^{119}\text{Sn}$  coherences is relatively long so that  $\sim 25$  spin echoes can be acquired, resulting in a further  $\sim 5$ -fold gain in signal-to-noise in comparison to standard CP acquisition. With the combined effects of signal enhancement from DNP (here  $\epsilon_{\text{H}} = \epsilon_{\text{Sn-CP}} = 30$ ), Boltzmann polarization from the 105 K sample temperatures (factor of 2.7), CPMG acquisition of  $^{119}\text{Sn}$  signals (factor of  $\sim 5$ ), and the reduction of the NMR signal by paramagnetic signal quenching (factor of 0.3) and by dilution of the sample (factor of 0.5), we estimate that the overall gain in sensitivity<sup>34</sup> with DNP-SENS should be on the order of a factor of 60.

For  $\text{Sn}/\text{SnO}_x$  NPs capped with organic ligands, the DNP enhancement factor for protons was around 30. High-quality DNP-SENS CP-CPMG spectra of the 10 and 18 nm particles were recorded in less than 1 h each (1000 scans, 3.5 s recycle delay). In the same experiment, but without microwaves, the signal was below the noise level even after 512 scans, which shows that the DNP-enhanced proton polarization was successfully transferred to the surface  $^{119}\text{Sn}$  nuclei. Importantly, the DNP-SENS spectrum of the 18 nm particles possesses a high signal-to-noise ratio after 1 h of signal averaging, while 21 h of signal averaging is required to obtain a weak signal in a conventional  $^{119}\text{Sn}$  direct pulse-acquired solid-state NMR experiment (Figure S3).

We observe a single broad peak centered at  $-597.3$  ppm for 10 nm NPs (Figure 1B) and at  $-603.4$  ppm for 18 nm NPs (Figure 1C). This chemical shift is consistent with the reference measurement of crystalline  $\text{SnO}_2$  (Figure S4). With DNP-SENS, no other signals were observed between 800 and  $-400$  ppm (Figure 1D,E), thus indicating the absence of detectable  $\text{SnO}$  in the outer part of the NPs. The  $^1\text{H}$ – $^{119}\text{Sn}$  2D HETCOR NMR spectra (Figure 1A) indicate correlations between  $\text{SnO}_2$  from the surface of the particles and the protons of the oleic acid (methylene protons with  $^1\text{H}$  chemical shifts of 2.5 ppm) and the solvent (1,1,2,2-tetrachloroethane,  $^1\text{H}$  chemical shift of 6.1 ppm), in agreement with the expected mechanism for proton-mediated polarization transfer. In addition to  $^{119}\text{Sn}$  NMR data, 1D  $^{13}\text{C}$  CPMAS DNP-SENS experiments (Figure S5) show successful signal enhancement also for oleate capping, and the results are in full agreement with the FTIR assignments, pointing to the absence of the free oleic acid.

DNP-SENS  $^{119}\text{Sn}$  CP-CPMG spectra show line widths of  $\sim 65$  ppm. It is interesting to note that the line width is similar for both 10 and 18 nm  $\text{Sn}/\text{SnO}_x$  NPs and is broader than any previously reported value in the literature. For instance, crystalline 4 nm  $\text{SnO}_2$  NPs exhibit line widths of  $\sim 25$  ppm, while crystalline but hollow  $\text{SnO}_2$  nanospheres with a wall thickness of  $\sim 3$  nm exhibit line widths of 54 ppm.<sup>35</sup> For comparison, a much narrower line width (1.7 ppm) is measured



for commercial, highly crystalline 50 nm SnO<sub>2</sub> powders (Figure S4), and line widths <5 ppm are reported in bulk SnO<sub>2</sub>.<sup>36</sup> We thus conclude that the line broadening of our NMR spectra arises from the amorphous nature of the SnO<sub>2</sub> layer combined with inhomogeneities at the NP surface and at the SnO/SnO<sub>2</sub> interfaces. This conclusion is supported by XRD and TEM data, showing only one crystalline phase, the metallic tin core, present in the particles. To the best of our knowledge, there are no published <sup>119</sup>Sn NMR studies concerning nanosized amorphous SnO<sub>2</sub>, possibly because phase-pure, unsupported SnO<sub>2</sub> particles always tend to be crystalline.

DNP-SENS can be also used to enhance the <sup>119</sup>Sn signals for highly hydrophilic, inorganic-capped Sn/SnO<sub>x</sub> NPs obtained by replacing the oleate capping with sulfide ions.<sup>1</sup> For this experiment, we used AMUPol,<sup>24</sup> a water-soluble biradical which was reported to enhance <sup>1</sup>H NMR spectra by the factor of up to 235 in glycerol-*d*<sub>8</sub>/D<sub>2</sub>O/H<sub>2</sub>O mixture. In our experiment, an equivalent volume of a 16 mM solution of AMUPol in DMSO-*d*<sub>6</sub>/D<sub>2</sub>O/H<sub>2</sub>O (60:36:4) was mixed with inorganic-capped Sn/SnO<sub>x</sub> NPs dispersed in DMSO-*d*<sub>6</sub>/H<sub>2</sub>O (60:40) solvent mixture. The final mass fraction of the protonated solvent (H<sub>2</sub>O) was around 22%. The  $\epsilon_H$  was  $\sim 11$  (Figure 2A), and we were able to clearly resolve <sup>119</sup>Sn DNP-SENS signals at  $-603$  ppm, with a signal-to-noise ratio of  $\sim 18$ .<sup>25,26</sup> No signal could be detected in the region relevant to SnO (Figure 2B). This result on sulfide-capped colloids highlights the applicability of DNP-SENS for both types of inorganic colloids: organic-capped NPs dispersed in nonpolar solvents and highly hydrophilic, inorganic-capped NPs dispersed in highly polar solvent media.

In the past, synchrotron radiation photoemission studies<sup>37</sup> and electron energy loss spectroscopy<sup>38</sup> elucidated that tin foil under ambient conditions or under 1 bar of O<sub>2</sub> is covered with a 1.7–3 nm oxide shell (thicker after air exposure), composed of SnO overlaid with SnO<sub>2</sub>. The deeper oxidation under air was attributed to the effect of moisture.<sup>38</sup> Indeed, Chaudret *et al.* have synthesized deeply oxidized Sn/SnO<sub>x</sub> NPs by decomposing [ $\{\text{Sn}(\text{NMe}_2)_2\}_2$ ] in anisole/water mixtures and could detect SnO phases from XRD measurements.<sup>39</sup> We therefore hypothesize that our Sn/SnO<sub>x</sub> NPs, synthesized in air- and moisture-free conditions and oxidized only by exposure to ambient atmosphere, should contain an amorphous SnO phase. However, SnO NMR signals are not observed by the DNP-SENS experiments, suggesting that SnO might be sandwiched between Sn and SnO<sub>2</sub> and, therefore, is inaccessible with DNP-SENS NMR. Note that we also attempted direct <sup>119</sup>Sn DNP-enhanced CPMG experiments in order to enhance NMR signals from subsurface SnO phases.<sup>40</sup> However, no signal was observed, likely because of lengthy <sup>119</sup>Sn longitudinal relaxation times and/or that signals from the SnO phase are very

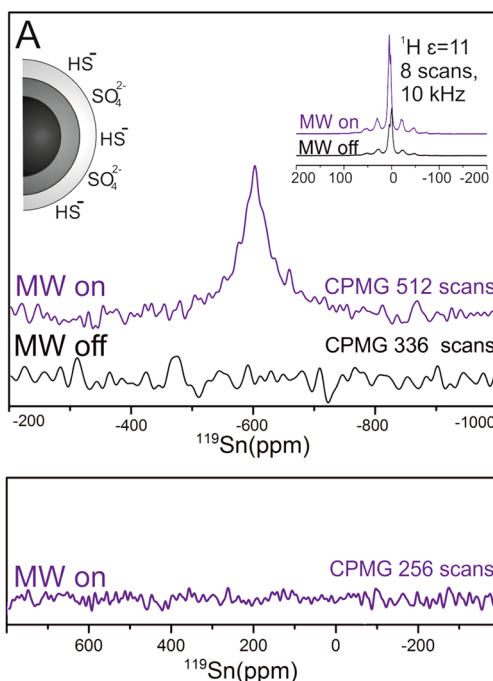


**Figure 2.** (A) MAS <sup>119</sup>Sn DNP-SENS NMR spectra for inorganic-capped 18 nm Sn/SnO<sub>x</sub> NPs suspended in an AMUPol solution in DMSO-*d*<sub>6</sub>/D<sub>2</sub>O/H<sub>2</sub>O ( $\sim 60:18:22$ ); MW off (black line, 336 scans, 7 s recycle delay) and MW on (dark blue, 512 scans, 7 s recycle delay) CP-CPMG echo reconstructed <sup>119</sup>Sn solid-state NMR spectra. Inset represents the MW off/MW on experiment for <sup>1</sup>H. (B) Illustration of the lack of detectable signal in the region relevant to SnO.

broad. We thus employed Mössbauer and X-ray absorption spectroscopies to test our hypothesis about the presence of subsurface SnO.

**Mössbauer Spectroscopy.** <sup>119</sup>Sn Mössbauer spectroscopy traditionally serves as a highly sensitive tool for determining the oxidation state and chemical environment of Sn atoms in solid-state materials, including ultrathin and amorphous structures, as well as NPs.<sup>39,41,42</sup> Two experimentally measured parameters are characteristic: the isomer shift (IS) and quadrupolar splitting (EQ). IS reflects the changes to the electronic density of *s*-electrons, caused by electron-donating or electron-withdrawing groups and, even more significantly, by the change in the oxidation state. EQ reflects the local spherical symmetry about the Sn center, with asymmetric environments possessing correspondingly large splitting of the nuclear energy levels. For <sup>119</sup>Sn, two substates are generated by quadrupolar splitting. Usually,  $\beta$ -Sn appears as a singlet with IS  $\approx 2.6$  mm  $\cdot$  s<sup>-1</sup> (Figure S6A) with a relative transmission intensity that is strongly dependent on the measurement temperature according to the thermal variation of the Lamb–Mössbauer *f* factor of <sup>119</sup>Sn nuclei.<sup>43</sup> The  $\alpha$ -SnO component shows an asymmetric quadrupole doublet with a large quadrupole splitting (1.4 mm  $\cdot$  s<sup>-1</sup>).<sup>39</sup> Finally, SnO<sub>2</sub> gives a quadrupole doublet with isomeric shift around 0–0.31 mm  $\cdot$  s<sup>-1</sup> (Figure S6B).

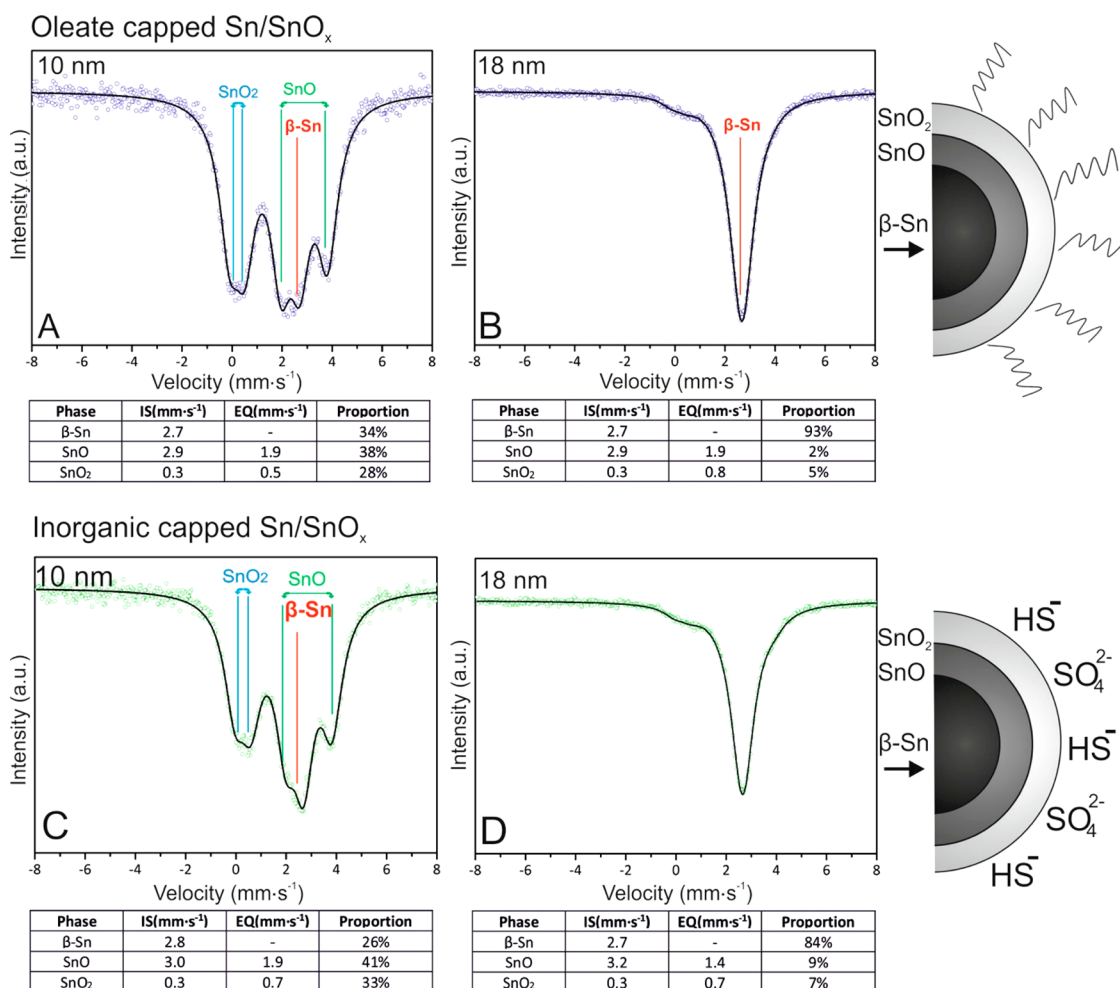


**Figure 3.** <sup>119</sup>Sn Mössbauer spectra recorded at 5 K, together with calculated phase composition for oleate-capped (A) 10 nm and (B) 18 nm Sn/SnO<sub>x</sub> NPs, and for inorganic capped counterparts (C,D). Solid lines represent the fitted spectra for three possible Sn species: β-Sn, α-SnO, and SnO<sub>2</sub>.

The Mössbauer spectra for 10 and 18 nm Sn/SnO<sub>x</sub> NPs, capped with organic and inorganic ligands, are presented in Figure 3. The peak areas yield the relative amounts of each Sn species. As expected, smaller NPs exhibit a higher degree of oxidation with up to 62% of the total Mössbauer signal intensity arising from the oxide phases. Most importantly, a high content (38% of the total signal) of SnO with IS = 2.9 mm·s<sup>-1</sup> is unambiguously detected, providing the first evidence for this phase which is not detected by electron microscopy or by NMR. The atomic proportion of oxides increases for NPs subjected to the ligand-exchange procedure. As expected, 18 nm NPs also exhibit both oxide phases but in much lower concentration for both organic and inorganic capped NPs: 2% (9%) for SnO and 5% (7%) for SnO<sub>2</sub> for NPs with organic and inorganic (numbers in brackets) surface capping.

**XAS Spectroscopy.** X-ray absorption spectroscopy (XAS) allows the study of the local electronic and geometric structure (up to 6 Å) around Sn atoms. XAS is an element-specific technique that does not rely on long-range order and has been extensively used to

study nanostructured Sn-oxide materials.<sup>44–48</sup> The X-ray absorption near edge structure (XANES) spectrum (–50 to 100 eV around the absorption edge) corresponds to the empty density of p states and, therefore, provides information about the structure, the oxidation state, and the site symmetry. Background-corrected and normalized Sn K-edge XANES spectra for 10 and 18 nm Sn/SnO<sub>x</sub> NPs are presented along with the reference, commercially available powders of Sn, SnO, and SnO<sub>2</sub> (Figure 4). As expected, the shift of the absorption edge toward higher energies, corresponding to higher oxidation state (SnO<sub>2</sub>), is more pronounced for smaller nanoparticles due to higher SnO and SnO<sub>2</sub> contents. Quantitatively, the content of Sn, SnO, and SnO<sub>2</sub> can be determined by linear combination fitting of the whole XAS spectrum using spectra of Sn, SnO, and SnO<sub>2</sub> as references (see an example of the fit in Figure 4C and Table S1 of the Supporting Information for phase composition of each sample). Qualitatively, a strong correlation is observed between the Mössbauer and XAS results: the proportion of SnO and SnO<sub>2</sub> oxides increases by several

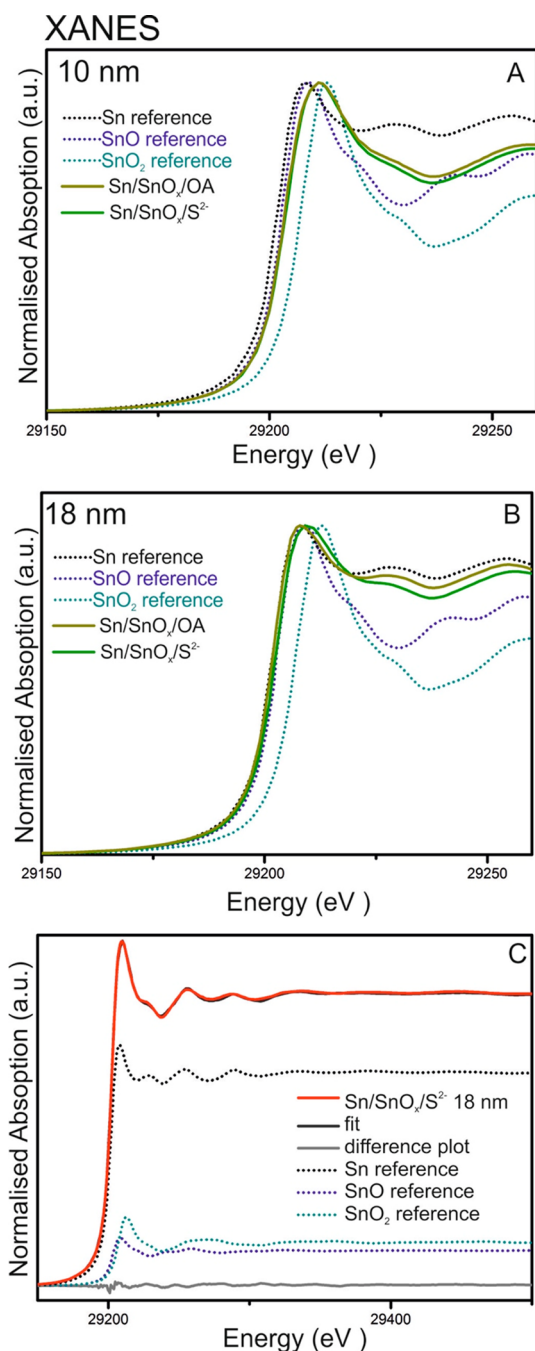


**Figure 4.** (A,B) Sn K-edge XANES spectra for 10 and 18 nm Sn/SnO<sub>x</sub> NPs along with spectra of Sn, SnO, and SnO<sub>2</sub> reference compounds. (C) Representative fit of the XAS spectrum for 18 nm Sn/SnO<sub>x</sub> NPs capped with inorganic (S<sup>2-</sup>) ligands (solid red trace) obtained with a combination of the reference Sn, SnO, and SnO<sub>2</sub> spectra (dotted traces). Table S1 (see Supporting Information) provides the fitting results in the form of weight percentage of each phase for 10 and 18 nm Sn/SnO<sub>x</sub> capped with organic and inorganic ligands.

percent upon ligand exchange, for both 10 and 18 nm oleate-capped NPs.

**Temperature-Dependent XRD Patterns.** In this section, we point the attention of the readers to the crystalline metallic ( $\beta$ -Sn) core of Sn/SnO<sub>x</sub> NPs. Using synchrotron X-ray diffraction patterns (60 keV X-ray photons; see

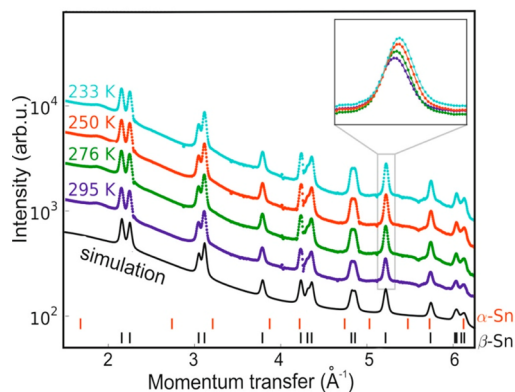


**Figure 5.** Synchrotron X-ray powder diffraction patterns for 18 nm Sn/SnO<sub>x</sub> NPs recorded at 233–295 K. The plot shows the scattered intensity versus the momentum transfer  $Q$  measured with 60 keV X-ray photons. The inset illustrates the thermal shift of the {132} Bragg diffraction peak.

Supporting Information for experimental details) recorded at various temperatures, we aimed to observe whether there is a transition from metallic  $\beta$ -Sn to semiconducting  $\alpha$ -Sn, which normally occurs at less than 13 °C in bulk Sn.<sup>49–52</sup> This question is also of high relevance for the potential use of nano-Sn in Li-ion batteries, which are required to operate reliably below 0 °C. Diffraction experiments were performed upon cooling from room temperature to 233 K (–40 °C, Figure 5, shown for 18 nm Sn/SnO<sub>x</sub> NPs). We chose 233 K because the fastest  $\beta$ -to- $\alpha$  conversion rates have previously been reported to occur at this temperature.<sup>28</sup> The observed Bragg peaks could be indexed by a  $\beta$ -Sn phase with lattice parameters in agreement with the bulk values.<sup>53</sup> Simulation with the Rietveld method fully reproduces the experimental pattern if a crystalline  $\beta$ -Sn phase is used as the only component. The inset in Figure 5 shows the shift of the {132} Bragg peak due to thermal expansion, with a linear expansion coefficient identical to that of bulk  $\beta$ -Sn. The speed of the phase transformation can be very slow (sometimes years)<sup>50,52</sup> and has been also reported to depend on the particle size.<sup>50,51</sup> Hence this transition could have been left undetected by Mössbauer spectroscopy at the temperature of 5 K, for which the time scale of the measurements falls in the sub-24 h range. We therefore remeasured XRD patterns for the samples kept at 255 K for 24 h, showing no signs of phase transition. Moreover, we stored the samples in a freezer at  $\sim$ 255 K (–18 °C) for a period of 8 months and again observed identical XRD patterns (Figure S7). Finally, we compared our NPs with larger, commercially available Sn particles with mean grain sizes of 100 nm and 10  $\mu$ m, subjected to the same 8 months of cold storage. In all samples, the bulk  $\beta$ -Sn structure is retained. We therefore conclude that sub-10 nm Sn crystallites and the bulk material do not exhibit any substantial difference in the phase diagram or recrystallization kinetics.

## CONCLUSIONS

The combined analysis of DNP-SENS with TEM, Mössbauer, and XAS spectroscopies and XRD is consistent with a core/shell1/shell2 model of Sn/SnO/SnO<sub>2</sub> NPs capped with organic and inorganic ligands, where the only crystalline constituent is the metallic  $\beta$ -Sn core. Importantly, low-temperature XRD measurements after 8 months cooling at 255 K did not detect any phase transition to a brittle  $\alpha$ -Sn phase. The utility of DNP-SENS for analyzing the highly disordered, outermost layers of the NP cores irrespective of the chosen ligand capping (organic or inorganic) is demonstrated using naturally oxidized, highly monodisperse 10 and 18 nm Sn/SnO<sub>x</sub> NPs as a case study. The broadening of the <sup>119</sup>Sn NMR spectra is reflective of the degree of atomic disorder. For

example, highly crystalline 50 nm SnO<sub>2</sub> yields <sup>119</sup>Sn NMR signals with line widths of about 1–2 ppm, while line widths of up to 70 ppm were found for the amorphous SnO<sub>2</sub> layer at the surface of the 10 and 18 nm Sn/SnO<sub>x</sub> NPs. DNP-SENS holds great promise to address various research problems in contemporary nanomaterials research: organic and inorganic surface chemistry, radially resolved chemical and phase composition of NPs (as shown in this study), distribution of dopants and impurities, correlation between electronic effects (quantum size effects, surface plasmons) with the chemical shift in NMR spectra, etc. The only limitation of DNP-SENS is that it is rather restricted to those materials which contain NMR-sensitive nuclei with sufficient abundance, preferably with a spin of 1/2.

## EXPERIMENTAL SECTION

**Sn/SnO<sub>x</sub> NPs.** Sn/SnO<sub>x</sub> NPs (10 and 18 nm) were synthesized, purified, and surface-modified with oleate or with inorganic ligands according to our recently published methods.<sup>1</sup> For the organic-to-inorganic ligand exchange, we used *n*-methylformamide/hexane phase transfer solvent system and K<sub>2</sub>S as an inorganic capping agent.

**Conventional ambient temperature MAS <sup>119</sup>Sn solid-state NMR experiments** were performed on Bruker AMX400 spectrometer using a 2.5 mm zirconia rotors and a MAS frequency of 20 kHz. The spectral frequency was set at 149.25 MHz, and a 90° pulse length of 0.3  $\mu$ s was used. The relaxation delay was 2 s, and the number of scans was 38 231. All spectra were referenced to tetramethyltin ( $\delta_{\text{iso}} = 0.0$  ppm) via a secondary standard of tetracyclohexyltin ( $\delta_{\text{iso}} = -93$  ppm).

**DNP solid-state NMR experiments** were performed with a wide-bore 400 MHz Bruker Avance III spectrometer equipped with a 263 GHz gyrotron microwave source and a 3.2 mm low-temperature MAS probe.<sup>21</sup> The sweep coil of the main magnetic field was set so that microwave irradiation occurred at the positive <sup>1</sup>H enhancement maximum of the nitroxide biradicals (see Supporting Information for details of NMR experiments and sample preparation).

**<sup>119</sup>Sn Mössbauer measurements** were carried out using a constant-acceleration spectrometer in standard transmission geometry and a Ba<sup>119m</sup>SnO<sub>3</sub> source (~10 mCi) kept at room temperature. Spectra were recorded at 5 K in a liquid helium cryostat. A polycrystalline absorber with natural abundance of <sup>119</sup>Sn isotope and thickness of  $\approx 15$  mg cm<sup>-2</sup> was used. A palladium foil of 0.5 mm thickness was used as a critical absorber for Sn X-rays. The velocity scale was calibrated with a <sup>57</sup>CoRh source (25 mCi) and a metallic iron foil at room temperature. The <sup>119</sup>Sn isomer shifts are referenced to BaSnO<sub>3</sub> at room temperature. The Mössbauer spectra were fitted with a least-squares method program assuming Lorentzian peaks. The error on all the <sup>119</sup>Sn Mössbauer spectra is  $\pm 0.1$  mm  $\cdot$  s<sup>-1</sup>.

**Synchrotron X-ray powder diffraction measurements** were performed at the powder diffraction beamline P02.1 at Petra III/Hasylab, Hamburg, using 60 keV X-ray photons. Data collection was done with a Perkin-Elmer XRD1621 two-dimensional detector at a distance of 1000 mm. The Sn/SnO<sub>x</sub> NPs and commercial Sn powders were transferred into Kapton capillaries, and the measurements were performed in transmission geometry. The *in situ* cooling was obtained by a stream of cryogenic N<sub>2</sub>, heated to the desired temperature.

**X-ray absorption spectroscopy** was carried out at the X10DA (Super XAS) beamline at the Swiss Light Source, Villigen, Switzerland. Spectra were collected on pressed pellets optimized to 1 absorption length at the Sn K-edge (29200.1 eV) in transmission mode. The beamline energy axis was calibrated with a Sn reference foil. The spectra were background-corrected

and normalized at the height of the edge step using the iFEffit software package.<sup>54</sup> Linear combination fits were performed over the range of 29 150 to 29 500 eV using reference spectra of SnO, SnO<sub>2</sub>, and  $\beta$ -Sn.

**Attenuated total reflectance (ATR) FTIR** spectra were recorded using Thermo Scientific Nicolet iS5 FTIR spectrometer. Samples were deposited onto Si substrates, turned upside down, and pressed against diamond ATR crystal. Liquid samples were measured by placing a small droplet directly onto ATR crystal. **Scanning transmission electron microscopy (STEM)** investigations were performed on the aberration-corrected HD-2700CS (Hitachi; cold-field emitter), operated at an acceleration potential of 200 kV.

**Conflict of Interest:** The authors declare no competing financial interest.

**Acknowledgment.** We thank Dr. Frank Krumeich for the STEM measurements, Dr. Rene Verel for help with <sup>119</sup>Sn MAS NMR, and Dr. Maksym Yarema for SEM measurements. D.K. and J.S. acknowledge the help of A.C. Dippel and P. Walter at the synchrotron beamline P02 Desy Hamburg (XRD measurements). XAS measurements were performed at the SuperXAS beamline of the Swiss Light Source. We thank Prof. Paul Tordo, Dr. Olivier Ouar, and Dr. Gilles Casano (Aix-Marseille Université) for supplying the biradicals used in the DNP-SENS experiments. This work was supported in part by EQUIPEX contract ANR-10-EQPX-47-01, ERC Advanced Grant No. 320860, and ERC Starting Grant No. 306733. A.J.R. acknowledges support from an EU Marie-Curie IIF fellowship (PIIF-GA-2010-274574). M.V. acknowledges the support of SNF fellowship (200021\_143600). D.K. acknowledges the support by Austrian Academy of Sciences (DOC fellowship).

**Supporting Information Available:** Details of NMR experiments and additional figures. This material is available free of charge via the Internet at <http://pubs.acs.org>.

## REFERENCES AND NOTES

- Kravchyk, K.; Protesescu, L.; Bodnarchuk, M. I.; Krumeich, F.; Yarema, M.; Walter, M.; Guntlin, C.; Kovalenko, M. V. Monodisperse and Inorganically Capped Sn and Sn/SnO<sub>2</sub> Nanocrystals for High-Performance Li-Ion Battery Anodes. *J. Am. Chem. Soc.* **2013**, *135*, 4199–4202.
- Xu, L. P.; Kim, C.; Shukla, A. K.; Dong, A. G.; Mattox, T. M.; Milliron, D. J.; Cabana, J. Monodisperse Sn Nanocrystals as a Platform for the Study of Mechanical Damage during Electrochemical Reactions with Li. *Nano Lett.* **2013**, *13*, 1800–1805.
- Lesage, A.; Lelli, M.; Gajan, D.; Caporini, M. A.; Vitzthum, V.; Miéville, P.; Alauzun, J.; Roussey, A.; Thieuleux, C.; Mehdi, A.; et al. Surface Enhanced NMR Spectroscopy by Dynamic



- Nuclear Polarization. *J. Am. Chem. Soc.* **2010**, *132*, 15459–15461.
4. Lelli, M.; Gajan, D.; Lesage, A.; Caporini, M. A.; Vitzthum, V.; Mieville, P.; Heroguel, F.; Rascon, F.; Roussey, A.; Thieuleux, C.; *et al.* Fast Characterization of Functionalized Silica Materials by Silicon-29 Surface-Enhanced NMR Spectroscopy Using Dynamic Nuclear Polarization. *J. Am. Chem. Soc.* **2011**, *133*, 2104–2107.
  5. Rossini, A. J.; Zagdoun, A.; Lelli, M.; Lesage, A.; Copéret, C.; Emsley, L. Dynamic Nuclear Polarization Surface Enhanced NMR Spectroscopy. *Acc. Chem. Res.* **2013**, *46*, 1942–1951.
  6. Lovingood, D. D.; Achey, R.; Paravastu, A. K.; Strouse, G. F. Size- and Site-Dependent Reconstruction in CdSe QDs Evidenced by  $^{77}\text{Se}\{^1\text{H}\}$  CP-MAS NMR Spectroscopy. *J. Am. Chem. Soc.* **2010**, *132*, 3344–3354.
  7. Ratcliffe, C. I.; Yu, K.; Ripmeester, J. A.; Badruz Zaman, M.; Badarau, C.; Singh, S. Solid State NMR Studies of Photoluminescent Cadmium Chalcogenide Nanoparticles. *Phys. Chem. Chem. Phys.* **2006**, *8*, 3510–3519.
  8. Abraham, A.; Mihaliuk, E.; Kumar, B.; Legleiter, J.; Gullion, T. Solid-State NMR Study of Cysteine on Gold Nanoparticles. *J. Phys. Chem. C* **2010**, *114*, 18109–18114.
  9. Yesinowski, J. P. In *Solid State NMR*; Chan, J. C. C., Ed.; Springer: Berlin, 2012; Vol. 306, pp 229–312.
  10. Sachleben, J. R.; Colvin, V.; Emsley, L.; Wooten, E. W.; Alivisatos, A. P. Solution-State NMR Studies of the Surface Structure and Dynamics of Semiconductor Nanocrystals. *J. Phys. Chem. B* **1998**, *102*, 10117–10128.
  11. Sachleben, J. R.; Wooten, E. W.; Emsley, L.; Pines, A.; Colvin, V. L.; Alivisatos, A. P. NMR-Studies of the Surface-Structure and Dynamics of Semiconductor Nanocrystals. *Chem. Phys. Lett.* **1992**, *198*, 431–436.
  12. Hens, Z.; Martins, J. C. A Solution NMR Toolbox for Characterizing the Surface Chemistry of Colloidal Nanocrystals. *Chem. Mater.* **2013**, *25*, 1211–1221.
  13. Berrettini, M. G.; Braun, G.; Hu, J. G.; Strouse, G. F. NMR Analysis of Surfaces and Interfaces in 2-nm CdSe. *J. Am. Chem. Soc.* **2004**, *126*, 7063–7070.
  14. Maly, T.; Debelouchina, G. T.; Bajaj, V. S.; Hu, K.-N.; Joo, C.-G.; Mak-Jurkauskas, M. L.; Sirigiri, J. R.; van der Wel, P. C. A.; Herzfeld, J.; Temkin, R. J.; *et al.* Dynamic Nuclear Polarization at High Magnetic Fields. *J. Chem. Phys.* **2008**, *128*, 052211.
  15. Ni, Q. Z.; Daviso, E.; Can, T. V.; Markhasin, E.; Jawla, S. K.; Swager, T. M.; Temkin, R. J.; Herzfeld, J.; Griffin, R. G. High Frequency Dynamic Nuclear Polarization. *Acc. Chem. Res.* **2013**, *46*, 1933–1941.
  16. Song, C.; Hu, K.-N.; Joo, C.-G.; Swager, T. M.; Griffin, R. G. TOTAPOL: A Biradical Polarizing Agent for Dynamic Nuclear Polarization Experiments in Aqueous Media. *J. Am. Chem. Soc.* **2006**, *128*, 11385–11390.
  17. Matsuki, Y.; Maly, T.; Ouari, O.; Karoui, H.; Le Moigne, F.; Rizzato, E.; Lyubenova, S.; Herzfeld, J.; Prisner, T.; Tordo, P.; *et al.* Dynamic Nuclear Polarization with a Rigid Biradical. *Angew. Chem., Int. Ed.* **2009**, *48*, 4996–5000.
  18. Hall, D. A.; Maus, D. C.; Gerfen, G. J.; Inati, S. J.; Becerra, L. R.; Dahlquist, F. W.; Griffin, R. G. Polarization-Enhanced NMR Spectroscopy of Biomolecules in Frozen Solution. *Science* **1997**, *276*, 930–932.
  19. Gruning, W. R.; Rossini, A. J.; Zagdoun, A.; Gajan, D.; Lesage, A.; Emsley, L.; Coperet, C. Molecular-Level Characterization of the Structure and the Surface Chemistry of Periodic Mesoporous Organosilicates Using DNP-Surface Enhanced NMR Spectroscopy. *Phys. Chem. Chem. Phys.* **2013**, *15*, 13270–13274.
  20. Vitzthum, V.; Mieville, P.; Carnevale, D.; Caporini, M. A.; Gajan, D.; Coperet, C.; Lelli, M.; Zagdoun, A.; Rossini, A. J.; Lesage, A.; *et al.* Dynamic Nuclear Polarization of Quadrupolar Nuclei Using Cross Polarization from Protons: Surface-Enhanced Aluminium-27 NMR. *Chem. Commun.* **2012**, *48*, 1988–1990.
  21. Rosay, M.; Tometich, L.; Pawsey, S.; Bader, R.; Schauwecker, R.; Blank, M.; Borchard, P. M.; Cauffman, S. R.; Felch, K. L.; Weber, R. T.; *et al.* Solid-State Dynamic Nuclear Polarization at 263 GHz: Spectrometer Design and Experimental Results. *Phys. Chem. Chem. Phys.* **2010**, *12*, 5850–5860.
  22. Kiesewetter, M. K.; Corzilius, B.; Smith, A. A.; Griffin, R. G.; Swager, T. M. Dynamic Nuclear Polarization with a Water-Soluble Rigid Biradical. *J. Am. Chem. Soc.* **2012**, *134*, 4537–4540.
  23. Zagdoun, A.; Casano, G.; Ouari, O.; Schwaerzwalder, M.; Rossini, A. J.; Aussenac, F.; Yulikov, M.; Jeschke, G.; Coperet, C.; Lesage, A.; *et al.* Large Molecular Weight Nitroxide Biradicals Providing Efficient Dynamic Nuclear Polarization at Temperatures up to 200 K. *J. Am. Chem. Soc.* **2013**, *135*, 12790–12797.
  24. Sauvée, C.; Rosay, M.; Casano, G.; Aussenac, F.; Weber, R. T.; Ouari, O.; Tordo, P. Highly Efficient, Water-Soluble Polarizing Agents for Dynamic Nuclear Polarization at High Frequency. *Angew. Chem., Int. Ed.* **2013**, *52*, 10858–10861.
  25. Larsen, F. H.; Skibsted, J.; Jakobsen, H. J.; Nielsen, N. C. Solid-State QCPMG NMR of Low-Gamma Quadrupolar Metal Nuclei in Natural Abundance. *J. Am. Chem. Soc.* **2000**, *122*, 7080–7086.
  26. Lefort, R.; Wiench, J. W.; Pruski, M.; Amoureux, J. P. Optimization of Data Acquisition and Processing in Carr–Purcell–Meiboom–Gill Multiple Quantum Magic Angle Spinning Nuclear Magnetic Resonance. *J. Chem. Phys.* **2002**, *116*, 2493–2501.
  27. Bloembergen, N.; Rowland, T. J. On the Nuclear Magnetic Resonance in Metals and Alloys. *Acta Metall.* **1953**, *1*, 731–746.
  28. Zagdoun, A.; Casano, G.; Ouari, O.; Lapadula, G.; Rossini, A. J.; Lelli, M.; Baffert, M.; Gajan, D.; Veyre, L.; Maas, W. E.; *et al.* A Slowly Relaxing Rigid Biradical for Efficient Dynamic Nuclear Polarization Surface-Enhanced NMR Spectroscopy: Expeditious Characterization of Functional Group Manipulation in Hybrid Materials. *J. Am. Chem. Soc.* **2011**, *134*, 2284–2291.
  29. Ysacco, C.; Karoui, H.; Casano, G.; Le Moigne, F.; Combes, S.; Rockenbauer, A.; Rosay, M.; Maas, W.; Ouari, O.; Tordo, P. Dinitroxides for Solid State Dynamic Nuclear Polarization. *Appl. Magn. Reson.* **2012**, *43*, 251–261.
  30. Lafon, O.; Thankamony, A. S. L.; Rosay, M.; Aussenac, F.; Lu, X.; Trebosc, J.; Bout-Roumazelles, V.; Vezine, H.; Amoureux, J.-P. Indirect and Direct Si-29 Dynamic Nuclear Polarization of Dispersed Nanoparticles. *Chem. Commun.* **2013**, *49*, 2864–2866.
  31. Akbey, U.; Altin, B.; Linden, A.; Ozelik, S.; Gradzielski, M.; Oschkinat, H. Dynamic Nuclear Polarization of Spherical Nanoparticles. *Phys. Chem. Chem. Phys.* **2013**, *15*, 20706–20716.
  32. Carr, H. Y.; Purcell, E. M. Effects of Diffusion on Free Precession in Nuclear Magnetic Resonance Experiments. *Phys. Rev.* **1954**, *94*, 630–638.
  33. Meiboom, S.; Gill, D. Modified Spin-Echo Method for Measuring Nuclear Relaxation Times. *Rev. Sci. Instrum.* **1958**, *29*, 688–691.
  34. Rossini, A. J.; Zagdoun, A.; Lelli, M.; Gajan, D.; Rascon, F.; Rosay, M.; Maas, W. E.; Coperet, C.; Lesage, A.; Emsley, L. One Hundred Fold Overall Sensitivity Enhancements for Silicon-29 NMR Spectroscopy of Surfaces by Dynamic Nuclear Polarization with CPMG Acquisition. *Chem. Sci.* **2012**, *3*, 108–115.
  35. Indris, S.; Scheuermann, M.; Becker, S. M.; Šepelák, V.; Kruk, R.; Suffner, J.; Gyger, F.; Feldmann, C.; Ulrich, A. S.; Hahn, H. Local Structural Disorder and Relaxation in SnO<sub>2</sub> Nanostructures Studied by  $^{119}\text{Sn}$  MAS NMR and  $^{119}\text{Sn}$  Mössbauer Spectroscopy. *J. Phys. Chem. C* **2011**, *115*, 6433–6437.
  36. Cossement, C.; Darville, J.; Gilles, J. M.; Nagy, J. B.; Fernandez, C.; Amoureux, J. P. Chemical-Shift Anisotropy and Indirect Coupling in SnO<sub>2</sub> and SnO. *Magn. Reson. Chem.* **1992**, *30*, 263–270.
  37. De Padova, P.; Fanfoni, M.; Larciprete, R.; Mangiantini, M.; Priori, S.; Perfetti, P. A Synchrotron Radiation Photoemission Study of the Oxidation of Tin. *Surf. Sci.* **1994**, *313*, 379–391.
  38. Hoflund, G. B.; Corallo, G. R. Electron-Energy-Loss Study of the Oxidation of Polycrystalline Tin. *Phys. Rev. B* **1992**, *46*, 7110–7120.

39. Nayral, C.; Viala, E.; Fau, P.; Senocq, F.; Jumas, J.-C.; Maisonnat, A.; Chaudret, B. Synthesis of Tin and Tin Oxide Nanoparticles of Low Size Dispersity for Application in Gas Sensing. *Chem.—Eur. J.* **2000**, *6*, 4082–4090.
40. Lafon, O.; Rosay, M.; Aussejac, F.; Lu, X.; Trebosc, J.; Cristini, O.; Kinowski, C.; Touati, N.; Vezin, H.; Amoureux, J.-P. Beyond the Silica Surface by Direct Silicon-29 Dynamic Nuclear Polarization. *Angew. Chem., Int. Ed.* **2011**, *50*, 8367–8370.
41. de Kergommeaux, A.; Faure-Vincent, J.; Pron, A.; de Bettignies, R.; Malaman, B.; Reiss, P. Surface Oxidation of Tin Chalcogenide Nanocrystals Revealed by Sn-119-Mossbauer Spectroscopy. *J. Am. Chem. Soc.* **2012**, *134*, 11659–11666.
42. Lippens, P. E. Interpretation of the Sn-119 Mossbauer Isomer Shifts in Complex Tin Chalcogenides. *Phys. Rev. B* **1999**, *60*, 4576–4586.
43. Hohenemser, C. Measurements of Mossbauer Recoilless Fraction in Beta-Sn for 1.3 to 370 Degrees K. *Phys. Rev.* **1965**, *139*, A185–A196.
44. Grandjean, D.; Benfield, R. E.; Nayral, C.; Maisonnat, A.; Chaudret, B. EXAFS and XANES Study of a Pure and Pd Doped Novel Sn/SnO<sub>x</sub> Nanomaterial. *J. Phys. Chem. B* **2004**, *108*, 8876–8887.
45. Grandjean, D.; Benfield, R. E.; Nayral, C.; Erades, L.; Soullantica, K.; Maisonnat, A.; Chaudret, B. EXAFS and XANES Study of Two Novel Pd Doped Sn/SnO<sub>x</sub> Nanomaterials. *Phys. Scr.* **2005**, *T115*, 699–702.
46. Brito, G. E. S.; Briois, V.; Pulcinelli, S. H.; Santilli, C. V. EXAFS and XRD Study of the Structural Evolution during Isothermal Sintering of SnO<sub>2</sub> Xerogels. *J. Sol–Gel Sci. Technol.* **1997**, *8*, 269–274.
47. Mourao, H. A. J. L.; Avansi Junior, W.; Ribeiro, C. Hydrothermal Synthesis of Ti Oxide Nanostructures and TiO<sub>2</sub>: SnO<sub>2</sub> Heterostructures Applied to the Photodegradation of Rhodamine B. *Mater. Chem. Phys.* **2012**, *135*, 524–532.
48. Jiang, H.; Liu, X. F.; Zou, Z. Y.; Tang, R. H.; Liu, W.; Yu, R. H. Mediating Distribution of Magnetic Co Ions by Surfactant in Co-Doped SnO<sub>2</sub> Nanorods. *J. Nanosci. Nanotechnol.* **2013**, *13*, 1111–1115.
49. Bhattacharya, V.; Chattopadhyay, K. Morphology and Phase Transformation of Nanoscaled Indium-Tin Alloys in Aluminium. *Mater. Sci. Eng., A* **2004**, *375*, 932–935.
50. Plumbridge, W. J. Tin Pest Issues in Lead-Free Electronic Solders. *J. Mater. Sci.: Mater. Electron.* **2007**, *18*, 307–318.
51. Durdaller, C. G.; Pound, G. M.; Robinson, W. H. Nucleation Rates in Alpha to Beta Transformation of Tin. *Trans. Metall. Soc. AIME* **1964**, *230*, 193–200.
52. Iizumi, M. Real-Time Neutron-Diffraction Studies of Phase-Transition Kinetics. *Physica B & C* **1986**, *136*, 36–41.
53. Wyckoff, R. W. G. *Crystal Structures*, 2nd ed.; Interscience Publishers: New York, 1963.
54. Newville, M. IFEFFIT: Interactive XAFS Analysis and FEFF Fitting. *J. Synchrotron Radiat.* **2001**, *8*, 322–324.